



Measurement and modeling of ionization in a cesium diode pumped alkali laser (DPAL)

Benjamin Oliker¹ · Hal Cambier² · Greg Pitz³ · David A. Hostutler³ · Timothy Madden³ · Wolfgang Rudolph⁴

Received: 11 May 2024 / Accepted: 26 June 2024 / Published online: 6 July 2024
© The Author(s), under exclusive licence to Springer-Verlag GmbH Germany, part of Springer Nature 2024

Abstract

We report direct measurement of the laser induced ionization rate of cesium, relevant for a Diode Pumped Alkali Laser (DPAL), via application of an ion chamber diagnostic. Computer simulation predictions of the multi-step ionization mechanism will be compared against measured ionization rates. The results will be shown to accurately predict the low level of ionization to within an order-of-magnitude, as well as relative trends across pump intensities of 8–100 W/cm² and cesium densities of 0.3–2.2 × 10¹² cm⁻³. Comparison of fluorescence from 7P energy states with known direct excitation pathways and fluorescence from highly-excited 7D states suggests rapid mixing of high energy states. The application of 300 V on the ion chamber electrodes (sufficient to cause current saturation) has minimal impact on fluorescence. This supports the notion that Rydberg states are populated via a neutral particle process, rather than via electron/ion recombination, as has been previously suggested.

1 Introduction

A promising candidate in the development of high power, excellent beam quality, low size and weight, electrically-powered laser systems is the diode pumped alkali laser (DPAL). This system has broad applications in military, aerospace, communications, and scientific diagnostics. DPAL is the first "hybrid" laser system to be heavily researched [1–5]. This hybrid system combines the benefits of a gas phase gain medium (scalability and heat removal by gas flow) and laser diode pumping (efficiency and electrical energy source).

The DPAL gain medium is a mixture of typically 1–10 atm of buffer gas, commonly noble gas and hydrocarbons, and a few parts-per-million (ppm) of alkali or less, with lasers demonstrated in cesium, rubidium, and

potassium. The lasing process involves the three lowest energy states of the alkali, shown in Fig. 1 for cesium. The diode laser pump is tuned to the D₂ absorption line of the cesium, which causes excitation from 6S_{1/2} to 6P_{3/2}. Population is then transferred to the 6P_{1/2} state via buffer gas collisions. Finally, a population inversion is created between the 6P_{1/2} and 6S_{1/2} states, enabling stimulated emission via the D₁ transition.

The desired laser kinetics of DPALs involve only the three lowest levels. However, unwanted processes such as ionization, cf. Fig. 1, can reduce laser efficiency by decreasing the population in the upper laser state and increasing heat generation. Understanding of ionization processes is critical to ensuring the success of DPAL power scaling.

Laser induced ionization in buffered alkali gases has been observed and analyzed since before the invention of DPAL [6–9]. Concerns about ionization in DPALs were reduced initially through low power testing and analysis [10–14]. Concerns were reduced significantly further by demonstration of efficient CW lasing at high power, intensity, and alkali density with performance characteristics that were in agreement with simulations predicting negligible ionization [3].

Ionization testing and simulation at high power (1 kW - 2 kW) were performed by Wallerstein, who demonstrated agreement between fluorescence measurements of a potassium DPAL and predictions based on kinetic simulation

✉ Benjamin Oliker
benjamin.oliker@baesystems.us

¹ Space and Mission Systems, BAE Systems, Inc., 10 Longs Peak Dr., Broomfield, CO 80021, USA

² CHESS, Material Research Laboratory, University of Illinois at Urbana-Champaign, 104 S. Goodwin Ave., MC-230, Urbana, IL 61801, USA

³ Directed Energy Directorate, Air Force Research Laboratory, 3550 Aberdeen Dr. SE, Kirtland AFB, NM 87108, USA

⁴ Department of Physics and Astronomy, University of New Mexico, 210 Yale Blvd. NE, Albuquerque, NM 87106, USA

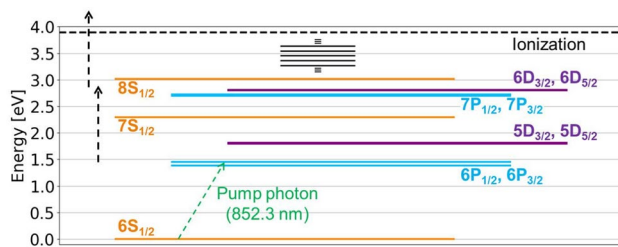


Fig. 1 The lowest 11 energy states of atomic cesium gas. The group of black horizontal lines represents the large density of states near the ionization threshold (3.89 eV). The dotted arrows indicate ionization pathways through collisions or photon absorption. Note the energy of a pump photon is 1.45 eV

[15]. The model was used to extrapolate to intensities of 100 kW/cm^2 and potassium densities of 10^{16} cm^{-3} , showing $< 10\%$ ionization throughout the parameter space. However, evidence of DPAL efficiency reduction due to ionization was observed by Zhdanov et al. [16]. The authors demonstrated significant output power increase in a potassium DPAL with 4% methane compared to pure helium buffer gas. Zhdanov et al., Waichman, and Cambier & Madden, have attributed this result to rapid quenching of excess kinetic energy in the free electron plasma by the hydrocarbon [17, 18]. The authors showed that a cycle of super-elastic collisions of free electrons and excited alkali, followed by electron impact ionization, becomes the dominant ionization process if energy removal from free-electrons is too slow.

Most previous experimental examinations of DPAL ionization have been indirect. The analysis has focused on explanation of observed laser behavior (such as output power, absorption, and fluorescence) with energy state rate equation modeling based on known processes. These investigations have shown evidence that ionization was the source of the observed changes; however, this approach can never instill the same level of confidence as a direct measurement. The examination described in this report include direct measurements of DPAL ionization rate using an ion chamber diagnostic.

There have been multiple investigations of ionization in a rubidium DPAL gain medium over the past decade [19–21], which involved a similar ion chamber setup to what is described in this report. However, the main difference is that the current effort is focused on measurement of the ionization rate; whereas, the previous efforts measured steady-state plasma density (resulting from a balance of ionization and recombination). The direct measurement of ionization rate in this report enables examination of the ionization processes, without the added complication of having to take into account electron/ion recombination and associated uncertainties [22].

The main objective of this paper is to evaluate the current understanding of ionization mechanisms that occur in

cesium DPAL by comparing direct ionization measurements to predicted rates based on known processes. In Sect. 2, an overview of the ion chamber and fluorescence measurements is provided. In Sect. 3, the theoretical basis for known laser-excited cesium ionization processes is examined and a predictive simulation of the total ionization rate inside the ion chamber diagnostic is described. In Sect. 4, the measurements using an ion chamber and fluorescence spectrometer are compared against predictions, and the results are analyzed in Sect. 5. Finally, conclusions are drawn in Sect. 6.

2 Experimental apparatus

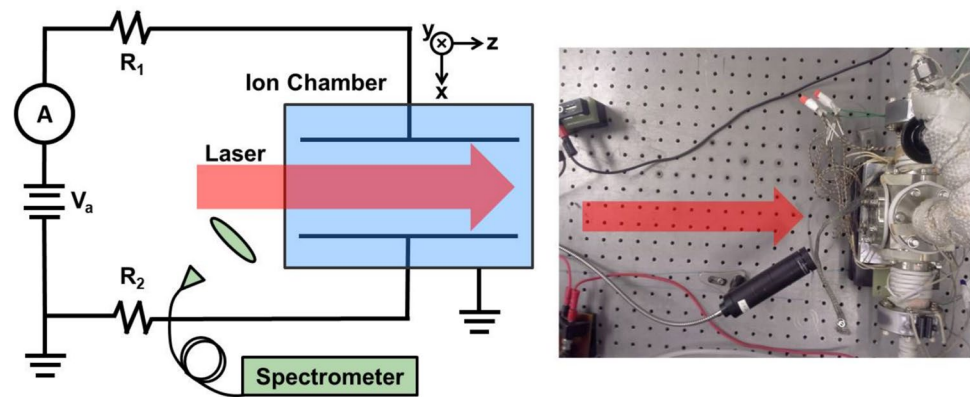
An ion chamber diagnostic has been used to measure the ionization rate inside a cesium DPAL gain medium. The diagnostic has been previously built, tested, and analyzed by the authors with results published separately [22].

An ion chamber is a common diagnostic in radiation dosimetry. The device consists of two electrodes surrounding a volume of gas, which is being ionized by incident radiation. The rate at which the gas is ionized creates a detectable change to conductivity. The chamber is operated in a voltage regime where current is saturated. This occurs for voltages that are sufficiently large to draw all charged particles to their respective electrodes with negligible recombination loss, yet low enough to prevent field-induced ionization. The measured saturation current is a direct measurement of the rate at which ion/electron pairs are generated within the gas, even under conditions of spatially nonuniform, high ionization rates [22].

The ion chamber used to measure the ionization rate of a DPAL gain medium contained two uncoated fused silica windows, which allowed a beam of 852.3 nm laser light to pass through the cell, exciting and ionizing cesium within the gas. The $L = 7.7 \text{ cm}$ beam propagation path was surrounded by plane parallel copper electrodes of length $L_e = 6.9 \text{ cm}$ (z -axis), height $H = 0.9 \text{ cm}$ (y -axis), and spacing of $d = 1.0 \text{ cm}$ (x -axis). The buffer gas in the cell was either pure helium or a 6:1 mixture of helium:methane; having a pressure of 700 torr at room temperature. The pump beam intensity profile incident on the cell was measured before and after each test, and the beam diameter corresponding to the $1/e^2$ point of a Gaussian fit was recorded to be $0.17 \text{ cm} \pm 15\%$. The beam was nearly collimated with a beam area that increased by about 5% through the ion chamber. A diagram and image of the ion chamber are shown in Fig. 2.

Fluorescence was measured from a small region near the front window of the ion chamber. The fluorescence light was focused by a 2.5-cm diameter, 5.0-cm focal length lens into a multimode fiber, then propagated into a 750-mm Czerny-Turner spectrometer (Acton SpectraPro 2750) with a liquid-nitrogen cooled CCD camera.

Fig. 2 Left: diagram of test apparatus including an ion chamber and fluorescence detector. $R_1 = 1.54 \text{ M}\Omega$, $R_2 = 1.48 \text{ M}\Omega$. Voltage supply with built-in ammeter, A , generates applied voltage, V_a . Electrode separation along the x -axis and laser propagation along the z -axis. Right: top view of the ion chamber apparatus indicating laser propagation axis and showing fiber-coupled fluorescence collector



The DPAL ion chamber diagnostic was operated in two ways that were uncommon: (1) higher ionization rate than typical usage and (2) localized ionization within the beam, rather than uniform radiation of the entire cell volume. These atypical cases were tested and modeled by Olikier et al. [22]. It was found that these factors required higher applied voltage to achieve current saturation, but did not alter the accuracy of the ionization measurements.

3 Simulation of laser-induced ionization in cesium

In this section, a model of the expected saturation current in an ion chamber measurement is developed, based on known cesium excitation processes. The rate constants of the processes described in this section are listed in the appendix.

Computational calculation was necessary due the complex interaction of many important energy states, and due to pump beam intensity variation along the propagation axis caused by absorption. The details of the simulation can be found in Ref. [23].

The simulation involved one-dimensional discretization along the laser propagation axis (z -axis) into a sufficiently large number of slices, n , of constant thickness, Δz . In each slice, the laser intensity $I(z_i)$ was assumed to be constant and the ionization rate $Q(z_i)$ was calculated via energy state kinetics. The decrease of laser intensity due to absorption was determined to obtain $I(z_{i+1})$ necessary for computing the ionization rate $Q(z_{i+1})$, and the change in the pump laser spectrum during propagation, caused by frequency dependent absorption, was included in the calculation. The beam was simulated as a uniform circular (flat-top) beam in the x and y axes with beam area $A_b = \pi r^2$, where r is the beam $1/e$ radius. The $1/e$ radius was used since a uniform beam at this radius has the same peak intensity as a Gaussian. The measured 5% increase in laser beam area across the cell was ignored since it was found to have a negligible impact.

The total current was the sum of the contributions from each cell multiplied by the laser beam area. Note that the propagation distance through the chamber is $L = n\Delta z = 7.7 \text{ cm}$.

$$I_{sat} = eA_b \sum_{i=1}^n Q(z_i)\Delta z. \quad (1)$$

The behavior of the laser excited gas in each slice was determined by solving a system of ordinary differential equations (ODEs). The inputs to the equations were incident spectrally-resolved pump power, beam diameter, cesium density, buffer gas composition, temperature, and pressure. The equations included the following processes: spectral pump absorption, fluorescence, spin-orbit mixing, quenching, energy pooling, Penning ionization, and photoionization. Solutions to the system of ODEs were steady-state populations for the eleven labelled energy states in Fig. 1, pump absorption, and ultimately, ionization rate density, $Q(z_i)$.

The rates for each excitation or relaxation process included in the simulation are provided in the appendix. As shown in Fig. 1, all ionization pathways start with absorption of a pump photon, which created a significant population of $6P_{3/2}$. (The $6P_{3/2}$ state efficiently spin-orbit mixed with $6P_{1/2}$ only in the presence of methane.) Next, photon or collisional excitation from the $6P$ states could occur to levels with similar energy, $7P$, $6D$, or $8S$. The collisional process is called energy pooling. The photon process has not been included in the simulation, since it was negligible at pressures near 1 atm and intensities $<100 \text{ W/cm}^2$ [11, 24]. The final ionization step can be photonic or collisional, called photoionization or Penning ionization, respectively. At the pump laser intensities of the experiment, the dominant ionization pathway was expected to involve (1) pump photon absorption, (2) energy pooling, and (3) Penning ionization.

The rates R (units cm^3/s) for collisional processes are related to the cross sections σ through the following equation. The values of σ used in the simulation are given in the appendix.

$$R = \sigma v_r(T) \tag{2}$$

where

$$v_r(T) = \sqrt{\frac{8kT}{\pi} \left(\frac{1}{m_1} + \frac{1}{m_2} \right)}. \tag{3}$$

Here $m_{1,2}$ is the mass of the collision partners [25].

Energy pooling cross-sections, σ_{ep} , that have not been previously measured were estimated using an empirical model developed by Wallerstein et al. [24]. In the model, ΔE is the energy defect, and faster rates occur for exothermic reactions compared to endothermic reactions.

$$\sigma_{ep} \approx \begin{cases} (3.58 \pm 1.8) \times 10^{-14} \exp[-0.71 \pm 0.28(\Delta E/kT)] \text{ cm}^2 & \text{if } \Delta E > 0 \\ (1.60 \pm 0.5) \times 10^{-14} \exp[+0.84 \pm 0.04(\Delta E/kT)] \text{ cm}^2 & \text{if } \Delta E < 0 \end{cases} \tag{4}$$

4 Ion chamber measurements

In this section we will compare measured saturation currents, I_{sat} , of laser-induced ionization in cesium gas using the ion chamber diagnostic, against predictions based on known cesium kinetic processes. This will allow for assessment of the validity of the models in Sect. 5.

Comparison of measurements and simulation with error analysis is shown in Figs. 3, 4 and 5. These data sets describe saturation current as a function of laser power and alkali density and illustrate the effect of buffer gas. All uncertainty bars correspond to a 1σ standard deviation.

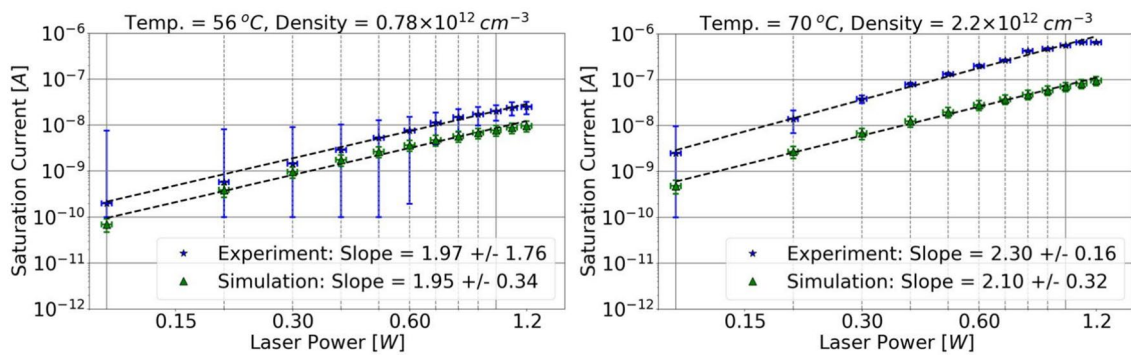


Fig. 3 Measured (blue stars) and simulated (green triangles) saturation current in an Cs ion chamber for different powers of the ionizing laser at low and high Cs density. The dashed lines are linear fits on

the log plots. Buffer gas was a 6:1 mixture of helium:methane with a pressure of 700 torr at room temperature

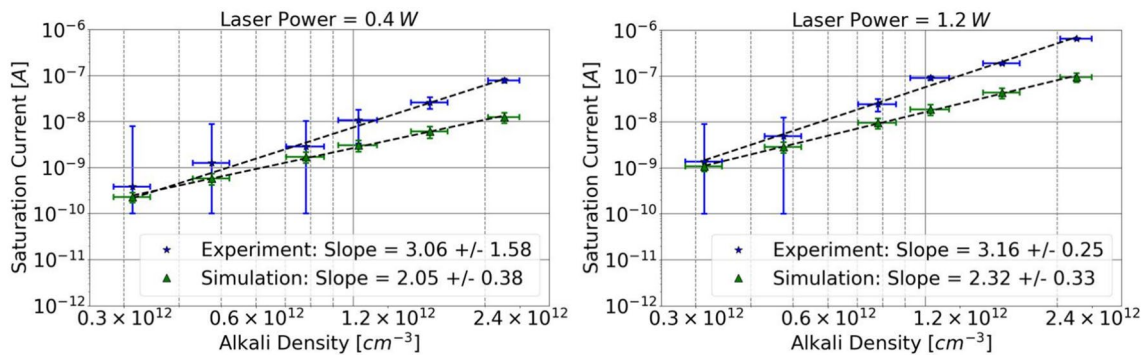


Fig. 4 Measured (blue stars) and simulated (green triangles) saturation current in an Cs ion chamber as a function of Cs density for two different laser powers. The dashed lines are linear fits on the log plots.

Buffer gas was a 6:1 mixture of helium:methane, and was 700 torr at room temperature

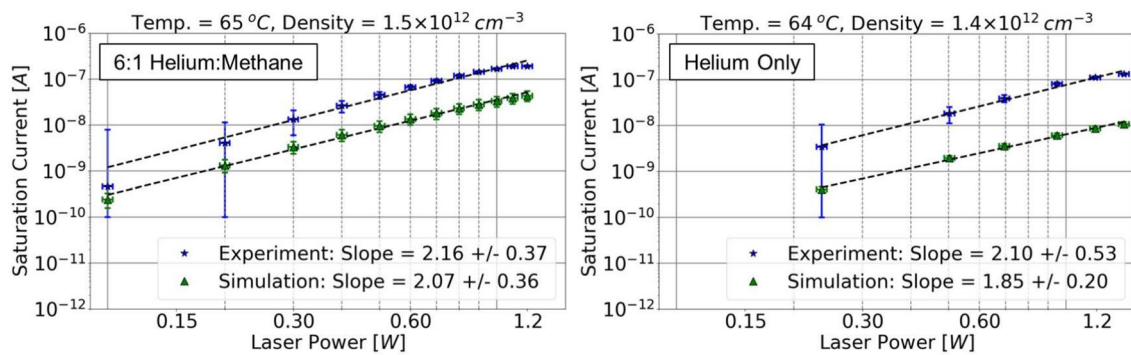


Fig. 5 Measured (blue stars) and simulated (green triangles) saturation current in an Cs ion chamber as a function of laser power for two similar Cs densities, but different buffer gas compositions. The

Uncertainty bars on measured saturation current, shown in Figs. 3, 4 and 5, was due to measurement noise and the variation of current above saturation. The latter were related to fluctuations in Cs vapor temperature and related density, laser power, and laser spectrum.

Uncertainty bars on simulated saturation current, shown in Figs. 3, 4 and 5, was due to uncertainty in experimental conditions input into the simulation. The following seven parameters were measured during testing and the associated error was quantified: pump spectrum center wavelength, pump spectral width (FWHM), buffer gas pressure, beam diameter, pump power, optical loss at windows, and cesium density. Note that the first six parameters were directly measured, and the seventh, cesium density, was calculated from measurements of pump transmission. The alkali densities based on transmission consistently corresponded to temperatures 1–5 °C hotter than thermocouple readings of the cell wall, indicating that the gas temperature inside the cell was slightly higher than the outer wall [26, 27]. Monte-Carlo analysis was performed to quantify the impact of uncertainty in these simulation inputs, resulting in uncertainty on the predicted saturation current. Details can be found in Ref. [23].

The goal of the comparison of experimental and simulation results was to evaluate the validity of the cesium ionization model, which was defined by the rate constants listed in the appendix. Because of this, uncertainty in the rate constants was not included in the Monte Carlo analysis, and did not contribute to the error bars on the predicted saturation current.

The maximum saturation current was measured at 650 nA \pm 2% and simulated at 100 nA \pm 45%, which occurred at a pump power of 1.2 W (0.97 W absorbed and peak intensity of 100 W/cm²) and a cesium density of 2.2×10^{12} cm⁻³. The measured rate is 6.5 \times higher than the simulated rate; however, both agree that ionization was a rare occurrence

dashed lines are linear fits on the log plots. The total pressure of both buffer gas mixtures was 700 torr at room temperature

with less than one ionization occurring for every one million absorbed pump laser photons.

The steady-state ion and electron populations have been simulated accounting for both recombination and mobility of the ions and electrons, published separately by the authors [22]. The rate constants used in the analysis for the helium/methane mixture was 1.0×10^{-7} cm³/s for bimolecular recombination and 8.7 cm²/Vs for ion mobility at 1 atm and 273 K. The peak ion density was 5.4×10^9 cm⁻³, which was 0.3% ionization.

Figure 3 shows that both experiment and simulation predicted a saturation current that increased quadratically with pump power, $I \propto P^2$. However, Fig. 4 shows that simulation and experiment produced different scaling of the saturation current with Cs density, demonstrating a quadratic and a cubic power dependence, respectively.

Figure 5 shows that the saturation current is about two times larger with a mixture of helium and methane as compared to helium only as buffer gas. The addition of methane produced a faster spin-orbit mixing of the 6P state. This resulted in a larger saturation current because of the larger population in the excited 6P states, producing a larger ionization rate.

4.1 Fluorescence measurements

Fluorescent lines were monitored simultaneously with the current measurements for three transitions, $7P_{3/2} \rightarrow 6S_{1/2}$ at 455 nm, $7P_{1/2} \rightarrow 6S_{1/2}$ at 459 nm, and $7D_{5/2} \rightarrow 6P_{3/2}$ at 697 nm.

The 7P states are shown in the cesium state diagram (Fig. 1) since these states were included in the ionization simulation. The 7P states are significantly populated via known energy pooling collisions.

Conversely, fluorescence was monitored from the 7D state, despite the fact that it was not included in the state

diagram or the ionization model. This was done to examine the behavior of states outside of the ionization model, particularly states that can be included in secondary energy pooling, as will be discussed further in Sect. 5.1. The $7D$ state has an energy of 3.23 eV, which is higher than any neutral state in the model.

The fluorescent power of all three transitions showed similar behavior when the laser power and cesium density were varied. The underlying quadratic and cubic power law dependencies resembled those of the saturation current discussed before.

Additionally, the fluorescence remained nearly constant with application of a bias voltage of 300 V, which was large enough to cause current saturation. This was observed for fluorescence from $7P$ and $7D_{5/2}$ states, as well as from highly excited states, $7G$ to $11D$ (with fluorescent lines from 530–575 nm). Fluorescent power was observed to decrease slightly with application of the bias voltage, with a maximum 20% at high pump power and high alkali density. This was likely due to slow diffusion of fresh cesium from around the beam to replace cesium ions pulled to the electrodes, which caused a localized decrease in the number of fluorescent particles.

5 Analysis and interpretation

Ion chamber measurements and simulation predictions agreed that ionization was rare with less than one ionization event per one million absorbed pump photons (<1 ppm). Relative changes in ionization rate showed agreement between prediction and measurement that saturation current increased as the square of the pump power. The relationship is cubic at low intensity and then decreases to quadratic at higher intensity due to saturation effects. The relationship is expected to drop below quadratic at higher intensity and higher saturation of the $6P$ states. The cubic dependence at small-signal is due to the interaction of three excited-state cesium atoms to cause ionization.

The dependence of the total current on alkali density was under-predicted by one order; the measured dependence was cubic, and the predicted dependence was quadratic. The total measured rates were up to $6.5\times$ larger at high alkali density and high pump power than the predicted rates. The following possible causes of the discrepancies between measurement and predictions have been investigated: (1) secondary energy pooling, (2) sensitivity of ionization to nonuniformity of the cesium gas, (3) effects of plasma transport to the electrodes, (4) radiation trapping, (5) Stark effect due to the applied electric field, and (6) inverse-bremsstrahlung photon absorption by the plasma.

Processes (3) to (6) can be ruled out based on the arguments given below; however, processes (1) and (2) will be scrutinized further in Sects. 5.1 and 5.2.

Radiation trapping is a process in which a fluorescence photon is re-absorbed elsewhere in the gas producing another fluorescence photon. This process can occur possibly multiple times. Radiation trapping is unlikely to have had a significant effect in our experiment since the pump absorption length of > 0.7 cm was longer than the beam diameter of about 0.2 cm.

The impact of perturbations of the cesium atoms due to the electric field, known as the Stark effect, were likely negligible. Generally, the Stark effect occurs when an applied electric field alters the energy states of a particle by pulling the electrons and nuclei in opposite directions. In the experiment, a maximum electric field of 500 V/cm was applied to the cesium gas, which is 6 orders-of-magnitude smaller than the field experienced by the ground-state valance electron due to the nucleus, which is approximately 214 MV/cm (based on a cesium atomic radius of 0.26 nm [28]). The calculated ionization potential decrease of cesium in the experiment due to the applied field of 500 V/cm is 0.4% from 3.89 to 3.87 eV, which is not expected to cause a significant change to 852 nm laser induced ionization [29].

Inverse-bremsstrahlung is a process that allows charged particles to absorb incident radiation. The process requires a collision partner to perturb and oscillate the charged particle, enabling it to accept the energy of the photon as increased kinetic energy. This effect is efficient at certain high plasma densities; however, it is minimal at the range of plasma densities in the experiment [30, 31].

5.1 Secondary energy pooling

We are considering secondary energy pooling, a collisional process between a $6P$ state and a higher energy state, resulting in the formation of a highly excited Rydberg state just below the ionization limit. This process could occur in collisions between the $6P$ states and either the $5D$ or $7S$ states, which would be formed after relaxing from higher states, $6D$, $7P$, and $8S$. We are referring to this process as secondary, since it occurs after an initial energy pooling collision generates population in the $6D$, $7P$, and $8S$ levels.

Such secondary energy pooling, or another collisional process, could account for the higher measured dependence of saturation current on cesium density. However, the collisional cross-sections for secondary energy pooling have been estimated in Table 1 and predict that the process is slow compared to Penning ionization from the $6D$, $7P$, and $8S$ states (see appendix). The rates have been calculated using Eq. (4), based on transitions from $5D$ to $8P$, $7D$, $9S$, $5F$, and $5G$, and from $7S$ to 74 different states from 3.68–3.84 eV.

Table 1 Estimated secondary energy pooling collision cross-sections based on Eq. (4) from Wallerstein et al. [24]

Secondary pooling reaction	Total cross-section [$\times 10^{-16}$ cm ²]
$6P_{1/2} + 5D_{3/2} \rightarrow Cs^{**} + 6S_{1/2}$	797
$6P_{3/2} + 5D_{3/2} \rightarrow Cs^{**} + 6S_{1/2}$	342
$6P_{1/2} + 5D_{5/2} \rightarrow Cs^{**} + 6S_{1/2}$	764
$6P_{3/2} + 5D_{5/2} \rightarrow Cs^{**} + 6S_{1/2}$	402
$6P_{1/2} + 7S_{1/2} \rightarrow Cs^{**} + 6S_{1/2}$	3712
$6P_{3/2} + 7S_{1/2} \rightarrow Cs^{**} + 6S_{1/2}$	7522

The energy states are based on transitions tabulated by Sansonetti [32].

Secondary energy pooling is unlikely to fully explain the difference between measured and predicted saturation current. However, it is likely to be the cause of two observations in fluorescence measurements.

First, this could explain why the dependence of fluorescence on cesium density from $7P$ and $7D$ was nearly the same. The $7P$ states can be populated directly by energy pooling from $6P$ collisions; whereas, $7D$ cannot. However, rapid mixing of Rydberg energy states by energy pooling would cause many states to have similar fluorescence dependence.

Second, fluorescence from Rydberg states was not significantly impacted by application of an electric field, which was sufficient to cause current saturation. This indicates that the Rydberg states are not populated by electron/ion recombination, as previously suggested [24], since current saturation indicates that recombination is negligible compared to drift of the charged particles to the electrodes. Instead, Rydberg states may be populated by collisions involving (neutral) Cs atoms, such as by secondary energy pooling.

5.2 Nonuniform distribution of Cs

Saturation current of the ion chamber was sensitive to density variations of the cesium gas, which was likely the dominant cause of discrepancies between measured and simulated results.

These density variations resulted from a nonuniform temperature distribution in the probed Cs vapor volume. Likely causes were condensation at windows and electrode surfaces, convection, and nonuniform heat exchange though the cell walls.

The range of cell temperatures investigated was 25 °C, which produced an order-of-magnitude change in average cesium density and three orders-of-magnitude change in saturation current. This exemplifies how sensitive the saturation current responds to changes in the Cs density, and

indicates that local maxima can increase the total current without changing total pump absorption. Nonuniformity of cesium gas is capable of accounting for both absolute differences between experimental and simulated saturation rates, and relative differences in the dependence on integrated cesium density.

In future testing, it is recommended to include a window along the beam path that can be used to image fluorescence and determine if any bright spots corresponding to dense cesium exist.

6 Conclusions

An ion chamber diagnostic was shown to be an effective tool in measurement of the laser induced ionization rate of a buffered cesium gas excited along the D_2 transition (852 nm), which is the typical setup of a cesium diode pump alkali laser (DPAL) gain medium. An ion chamber creates a direct measurement of ionization rate, since the saturation current is equal to the total rate that ion/electron pairs are generated in the gas volume. As such, this study was the first direct measurement of the ionization rate in a DPAL gain medium.

A DPAL ionization model was developed, and its results were compared against measurements using an ion chamber. The simulation was shown to predict the measured saturation current to within an order-of-magnitude at pump powers up to 1.2 W, peak intensities up to 100 W/cm², and average cesium densities up to 2.2×10^{12} cm⁻³.

The dominant ionization mechanism under the experimental conditions was simulated by three excitation steps: (1) pump photon absorption, (2) collisional energy pooling, and (3) collisional Penning ionization. Photon processes become increasingly dominant in multi-kilowatt DPAL systems with intensities of 1–10 kW/cm², and should be investigated further. These photon processes are off-resonant absorption and photoionization.

At the maximum pump laser power and cesium density, the measured saturation current was 650 nA and the simulation predicted 100 nA. The mostly likely cause of discrepancies between measured and simulated results was a nonuniform cesium density in the ion chamber. Experimental and simulation results were in agreement that the saturation current of the ion chamber had a roughly quadratic dependence on pump power over the range investigated, but were in disagreement on the dependence of saturation current on average cesium density; the measured dependence was roughly cubic and the predicted dependence was roughly quadratic.

Secondary energy pooling, a collisional excitation process resulting in excitation to near the ionization threshold, was further investigated with simultaneous fluorescence and ion chamber measurements. It was found that the process was unlikely to fully account for the difference between

measured and predicted ionization rates, but it is likely to be the process creating populations of high energy states observed in the fluorescence measurements.

Finally, fluorescence from Rydberg states was minimally affected by application of a 300 V electric field (sufficient for current saturation). This indicated that high energy states were populated via a neutral particle process, such as secondary energy pooling, rather than via electron/ion recombination, as has been previously suggested [24].

Appendix A: Simulation rate constants

Cross-sections used to determine kinetic rate constants in cesium excitation and ionization simulations are shown in Table 2. Fluorescence parameters including branching ratios are shown in Table 3.

Table 2 Cesium energy state kinetics parameters, listed as collision or photon cross-sections (σ)

Process	σ ($\times 10^{-16}$ cm ²)	Unc. ($\times 10^{-16}$ cm ²)	Temp. (K)	References
Spin-orbit mixing (methane)				
$6P_{3/2} + CH_4 \rightarrow 6P_{1/2} + CH_4$	21.36	0.01	298 K	[33, 34]
Quenching				
$6P_{1/2} + CH_4 \rightarrow 6S_{1/2} + CH_4$	0.019	Max.	313 K	[35]
$6P_{3/2} + CH_4 \rightarrow 6S_{1/2} + CH_4$	0.019	Max.	313 K	[35]
Energy pooling				
$26P_{1/2} \rightarrow 6S_{1/2} + 6D_{3/2}$	130	30	337–365 K	[36, 37]
$26P_{1/2} \rightarrow 6S_{1/2} + 6D_{5/2}$	80	40	337–365 K	[36]
$26P_{1/2} \rightarrow 6S_{1/2} + 7P_{1/2}$	38	18	337–365 K	[36]
$26P_{1/2} \rightarrow 6S_{1/2} + 7P_{3/2}$	13	4	337–365 K	[36]
$26P_{1/2} \rightarrow 6S_{1/2} + 8S_{1/2}$	0.33	0.17	337–365 K	[36]
$6P_{1/2} + 6P_{3/2} \rightarrow 6S_{1/2} + 6D_{3/2}$	49	Est.	350–597 K	[24, 38]
$6P_{1/2} + 6P_{3/2} \rightarrow 6S_{1/2} + 6D_{5/2}$	58	Est.	350–597 K	[24, 38]
$6P_{1/2} + 6P_{3/2} \rightarrow 6S_{1/2} + 7P_{1/2}$	2.4	Est.	350–597 K	[24]
$6P_{1/2} + 6P_{3/2} \rightarrow 6S_{1/2} + 7P_{3/2}$	4.7	Est.	350–597 K	[24]
$6P_{1/2} + 6P_{3/2} \rightarrow 6S_{1/2} + 8S_{1/2}$	4.6	Est.	350–597 K	[24]
$26P_{3/2} \rightarrow 6S_{1/2} + 6D_{3/2}$	27	9	337–365 K	[36, 37]
$26P_{3/2} \rightarrow 6S_{1/2} + 6D_{5/2}$	56	28	337–365 K	[36]
$26P_{3/2} \rightarrow 6S_{1/2} + 7P_{1/2}$	1.8	0.8	337–365 K	[36]
$26P_{3/2} \rightarrow 6S_{1/2} + 7P_{3/2}$	1.8	0.9	337–365 K	[36]
$26P_{3/2} \rightarrow 6S_{1/2} + 8S_{1/2}$	5.2	2.2	337–365 K	[36]
Penning ionization				
$Cs^{**} + 6P \rightarrow 6S_{1/2} + Cs^+ + e^-$	12,900	Est.	470 K	[39]
Photoionization				
$Cs^{**} + h\nu \rightarrow Cs^+ + e^-$	0.2	Est.	N/A	[11, 24] [40, 41]

The abbreviations Est. and Max. indicate an estimation and an upper bound, respectively

Table 3 Cesium fluorescence parameters

Symbol	Initial state	Final state	Rate [MHz]	Lifetime [ns]	Branching ratio	References
τ_{10}	$6P_{1/2}$	$6S_{1/2}$	28.6	34.9	1.0	[26, 32, 42, 43]
Total radiative lifetime [ns]				34.9		
τ_{20}	$6P_{3/2}$	$6S_{1/2}$	32.8	30.5	1.0	[26, 32, 42, 43]
Total radiative lifetime [ns]				30.5		
τ_{31}	$5D_{3/2}$	$6P_{1/2}$	0.913	1100	0.90	[32, 43, 44]
τ_{32}	$5D_{3/2}$	$6P_{3/2}$	0.107	9350	0.10	[32, 43, 44]
Total radiative lifetime [ns]				980		
τ_{42}	$5D_{5/2}$	$6P_{3/2}$	0.781	1280	1.0	[32, 43, 45]
Total radiative lifetime [ns]				1280		
τ_{51}	$7S_{1/2}$	$6P_{1/2}$	6.23	161	0.35	[43, 46]
τ_{52}	$7S_{1/2}$	$6P_{3/2}$	11.4	87.7	0.65	[43, 46]
Total radiative lifetime [ns]				56.7		
τ_{60}	$7P_{1/2}$	$6S_{1/2}$	0.793	1260	0.13	[32, 43, 47]
τ_{63}	$7P_{1/2}$	$5D_{3/2}$	1.59	629	0.27	[43, 46]
τ_{65}	$7P_{1/2}$	$7S_{1/2}$	3.52	284	0.60	[43, 46]
Total radiative lifetime [ns]				169		
τ_{70}	$7P_{3/2}$	$6S_{1/2}$	1.84	544	0.26	[32, 43, 47]
τ_{73}	$7P_{3/2}$	$5D_{3/2}$	0.13	7700	0.02	[43, 46]
τ_{74}	$7P_{3/2}$	$5D_{5/2}$	1.10	910	0.15	[43, 46]
τ_{75}	$7P_{3/2}$	$7S_{1/2}$	4.05	247	0.57	[43, 46]
Total radiative lifetime [ns]				140		
τ_{81}	$6D_{3/2}$	$6P_{1/2}$	12.7	78.7	0.82	[46]
τ_{82}	$6D_{3/2}$	$6P_{3/2}$	2.66	376	0.17	[46]
τ_{86}	$6D_{3/2}$	$7P_{1/2}$	0.090	11000	0.01	[46]
τ_{87}	$6D_{3/2}$	$7P_{3/2}$	0.0086	120000	0.00	[46]
Total radiative lifetime [ns]				64.7		
τ_{92}	$6D_{5/2}$	$6P_{3/2}$	15.2	65.8	1.00	[46]
τ_{97}	$6D_{5/2}$	$7P_{3/2}$	0.063	15870	0.00	[46]
Total radiative lifetime [ns]				65.5		
$\tau_{10,1}$	$8S_{1/2}$	$6P_{1/2}$	2.04	490	0.21	[46]
$\tau_{10,2}$	$8S_{1/2}$	$6P_{3/2}$	3.60	278	0.37	[46]
$\tau_{10,6}$	$8S_{1/2}$	$7P_{1/2}$	1.38	725	0.14	[46]
$\tau_{10,7}$	$8S_{1/2}$	$7P_{3/2}$	2.62	382	0.27	[46]
Total radiative lifetime [ns]				104		

Acknowledgements We thank Glen Perram at the Air Force Institute of Technology, Luke Emmert and Paul Schwoebel at the University of New Mexico, and Ryan Lane, Eric Guild, and Donald Stalnaker at the Air Force Research Laboratory. This effort was supported by the Directed Energy Professional Society, the Air Force Research Laboratory, and BAE Systems, Inc. The views expressed are those of the author and do not necessarily reflect the official policy or position of the Department of the Air Force, the Department of Defense, or the U.S. government.

Data availability The data that support the findings of this study is available from the corresponding author upon reasonable request.

References

1. W.F. Krupke, Diode-pumped alkali laser. Google Patents. US Patent 6,643,311 (2003)
2. R.J. Beach, W.F. Krupke, V.K. Kanz, S.A. Payne, M.A. Dubinskii, L.D. Merkle, End-pumped continuous-wave alkali vapor lasers: experiment, model, and power scaling. *JOSA B* **21**(12), 2151–2163 (2004)
3. G.A. Pitz, D.M. Stalnaker, E.M. Guild, B.Q. Olikier, P.J. Moran, S.W. Townsend, D.A. Hostutler, Advancements in flowing diode pumped alkali lasers. In: *High Energy/Average Power Lasers and Intense Beam Applications IX*, vol. 9729 (2016). International Society for Optics and Photonics

4. G.D. Hager, G.P. Perram, A three-level analytic model for alkali metal vapor lasers: Part I. Narrowband optical pumping. *Appl. Phys. B* **101**(1), 45–56 (2010)
5. B.V. Zhdanov, R.J. Knize, Review of alkali laser research and development. *Opt. Eng.* **52**(2), 021010 (2012)
6. R. Measures, Electron density and temperature elevation of a potassium seeded plasma by laser resonance pumping. *J. Quant. Spectrosc. Radiat. Transfer* **10**(2), 107–125 (1970)
7. A. Tam, G. Moe, W. Happer, Particle formation by resonant laser light in alkali-metal vapor. *Phys. Rev. Lett.* **35**(24), 1630 (1975)
8. L. Harris, Ionization and recombination in cesium-seeded plasmas near thermal equilibrium. *J. Appl. Phys.* **36**(5), 1543–1553 (1965)
9. C. Vadla, V. Horvatic, K. Niemax, Radiative transport and collisional transfer of excitation energy in Cs vapors mixed with Ar or He. *Spectrochim. Acta, Part B* **58**(7), 1235–1277 (2003)
10. S.S. Wu, Hydrocarbon-free resonance transition 795 nm rubidium laser. PhD thesis, San Diego, CA (2009)
11. R. Knize, B. Zhdanov, M. Shaffer, Photoionization in alkali lasers. *Opt. Express* **19**(8), 7894–7902 (2011)
12. B.Q. Oliker, J.D. Haiducek, D.A. Hostutler, G.A. Pitz, W. Rudolph, T.J. Madden, Simulation of deleterious processes in a static-cell diode pumped alkali laser. In: *High Energy/Average Power Lasers and Intense Beam Applications VII*, vol. 8962, p. 89620 (2014). International Society for Optics and Photonics
13. B. Barmashenko, S. Rosenwaks, M. Heaven, Static diode pumped alkali lasers: model calculations of the effects of heating, ionization, high electronic excitation and chemical reactions. *Opt. Commun.* **292**, 123–125 (2013)
14. A.H. Markosyan, M.J. Kushner, Plasma formation in diode pumped alkali lasers sustained in Cs. *J. Appl. Phys.* **120**(19), 193105 (2016)
15. A.J. Wallerstein, Kinetics of higher lying potassium states after excitation of the D_2 transition in the presence of helium. PhD thesis, Wright-Patterson Air Force Base, Ohio (2018)
16. B.V. Zhdanov, M.D. Rotondaro, M.K. Shaffer, R.J. Knize, Examination of potassium diode pumped alkali laser using He, Ar, CH_4 and C_2H_6 as buffer gas. *Opt. Express* **25**(24), 30793–30798 (2017)
17. K. Waichman, B.D. Barmashenko, S. Rosenwaks, Dependence of static K DPAL performance on addition of methane to He buffer gas: 3D CFD modeling and comparison with experimental results. *JOSA B* **36**(12), 3464–3470 (2019)
18. H.J. Cambier, T.J. Madden, Implementing and constraining higher fidelity kinetics for DPAL models. arXiv preprint <http://arxiv.org/abs/1902.10776> (2019)
19. L. Ge, W. Hua, H. Wang, Z. Yang, X. Xu, Study on photoionization in a rubidium diode-pumped alkali laser gain medium with the optogalvanic method. *Opt. Lett.* **38**(2), 199–201 (2013)
20. Z. Yang, L. Zuo, W. Hua, H. Wang, X. Xu, Experimental measurement of ionization degree in diode-pumped rubidium laser gain medium. *Opt. Lett.* **39**(22), 6501–6504 (2014)
21. X. Zhao, Z. Yang, W. Hua, H. Wang, X. Xu, Ionization degree measurement in the gain medium of a hydrocarbon-free rubidium vapor laser operating in pulsed and CW modes. *Opt. Express* **25**(8), 9458–9470 (2017)
22. B. Oliker, H. Cambier, H., Pitz, G., Hostutler, D.A., Madden, T., Rudolph, W., Analyzing the potential of ion chambers to measure laser-induced ionization rates. Preprint (2024)
23. B. Oliker, Examination of ionization in cesium diode pumped alkali lasers with an ion chamber diagnostic. PhD thesis, Albuquerque, NM (2022)
24. A.J. Wallerstein, G.P. Perram, C.A. Rice, Excitation of higher lying states in a potassium diode-pumped alkali laser. *Appl. Phys. B* **125**(8), 1–18 (2019)
25. G.A. Pitz, A.J. Sandoval, T.B. Tafoya, W.L. Klennert, D.A. Hostutler, Pressure broadening and shift of the rubidium D_1 transition and potassium D_2 transitions by various gases with comparison to other alkali rates. *J. Quant. Spectrosc. Radiat. Transfer* **140**, 18–29 (2014)
26. D.A. Steck, Cesium D line data. available online at <http://steck.us/alkalidata> (revision 2.2.1, 21 November 2019)
27. C. Alcock, V. Itkin, M. Horrigan, Vapour pressure equations for the metallic elements: 298–2500K. *Can. Metall. Q.* **23**(3), 309–313 (1984)
28. J.C. Slater, Atomic radii in crystals. *J. Chem. Phys.* **41**(10), 3199–3204 (1964)
29. C.E. Klots, R. Compton, Effects of uniform DC electric fields on multiphoton ionization of cesium atoms. *Phys. Rev. A* **31**(1), 525 (1985)
30. J. Dawson, C. Oberman, High-frequency conductivity and the emission and absorption coefficients of a fully ionized plasma. *Phys. Fluids* **5**(5), 517–524 (1962)
31. S. Pfalzner, P. Gibbon, Direct calculation of inverse-bremsstrahlung absorption in strongly coupled, nonlinearly driven laser plasmas. *Phys. Rev. E* **57**(4), 4698 (1998)
32. J. Sansonetti, Wavelengths, transition probabilities, and energy levels for the spectra of cesium (Cs I–Cs LV). *J. Phys. Chem. Ref. Data* **38**(4), 761–923 (2009)
33. G.A. Pitz, C.D. Fox, G.P. Perram, Transfer between the cesium $6^2P_{1/2}$ and $6^2P_{3/2}$ levels induced by collisions with H_2 , HD , D_2 , CH_4 , C_2H_6 , CF_4 , and C_2F_6 . *Phys. Rev. A* **84**(3), 032708 (2011)
34. E. Walentynowicz, R. Phaneuf, W. Baylis, L. Krause, Inelastic collisions between excited alkali atoms and molecules IX. an isotope effect in the cross sections for $6^2P_{1/2} \leftrightarrow 6^2P_{3/2}$ mixing in cesium, induced in collisions with deuterated methanes. *Can. J. Phys.* **52**(7), 584–588 (1974)
35. N.D. Zamoski, W. Rudolph, G.D. Hager, D.A. Hostutler, A study of collisional quenching and radiation-trapping kinetics for Rb (5P) in the presence of methane and ethane using time-resolved fluorescence. *J. Phys. B: At. Mol. Opt. Phys.* **42**(24), 245401 (2009)
36. Z. Jabbour, R. Namiotka, J. Huennekens, M. Allegrini, S. Milošević, F. De Tomasi, Energy-pooling collisions in cesium: $6P_j + 6P_j \rightarrow 6S + (nl=7P, 6D, 8S, 4F)$. *Phys. Rev. A* **54**(2), 1372 (1996)
37. T. Yabuzaki, A. Tam, M. Hou, W. Happer, S. Curry, Preferential excitation transfer in $Cs^*(6D_{3/2})$ - $Cs(6S_{1/2})$ collisions. *Opt. Commun.* **24**(3), 305–310 (1978)
38. C. Vadla, Energy pooling in caesium vapour. *Eur. Phys. J. D Atom. Mol. Opt. Plasma Phys.* **1**(3), 259–264 (1998)
39. L. Barbier, M. Chéret, Experimental study of penning and hornbeckmolnar ionisation of rubidium atoms excited in a high S or D level ($5D \leq nl \leq 11S$). *J. Phys. B: At. Mol. Phys.* **20**(6), 1229 (1987)
40. B. Duncan, V. Sanchez-Villicana, P. Gould, H. Sadeghpour, Measurement of the Rb ($5D_{5/2}$) photoionization cross section using trapped atoms. *Phys. Rev. A* **63**(4), 043411 (2001)
41. O. Zatsarinny, S. Tayal, Photoionization of potassium atoms from the ground and excited states. *Phys. Rev. A* **81**(4), 043423 (2010)
42. R. Rafac, C. Tanner, A. Livingston, K. Kukla, H. Berry, C. Kurtz, Precision lifetime measurements of the $6p^2P_{1/2,3/2}$ states in atomic cesium. *Phys. Rev. A* **50**(3), 1976 (1994)
43. K.C. Brown, G.P. Perram, Spin-orbit relaxation and quenching of cesium 7^2P in mixtures of helium, methane, and ethane. *Phys. Rev. A* **85**(2), 022713 (2012)
44. M. Safronova, C.W. Clark, Inconsistencies between lifetime and polarizability measurements in Cs. *Phys. Rev. A* **69**(4), 040501 (2004)
45. D. DiBerardino, C. Tanner, A. Sieradzan, Lifetime measurements of cesium $5d^2D_{5/2,3/2}$ and $11s^2S_{1/2}$ states using pulsed-laser excitation. *Phys. Rev. A* **57**(6), 4204 (1998)
46. O. Heavens, Radiative transition probabilities of the lower excited states of the alkali metals. *JOSA* **51**(10), 1058–1061 (1961)

47. A. Vasilyev, I. Savukov, M. Safronova, H. Berry, Measurement of the 6S - 7P transition probabilities in atomic cesium and a revised value for the weak charge Q_w . *Phys. Rev. A* **66**(2), 020101 (2002)

Publisher's Note Springer Nature remains neutral with regard to jurisdictional claims in published maps and institutional affiliations.

Springer Nature or its licensor (e.g. a society or other partner) holds exclusive rights to this article under a publishing agreement with the author(s) or other rightsholder(s); author self-archiving of the accepted manuscript version of this article is solely governed by the terms of such publishing agreement and applicable law.